

# Automated Segmentation of Cells With IHC Membrane Staining

Elisa Ficarra, *Member, IEEE*, Santa Di Cataldo\*, *Student Member, IEEE*,  
Andrea Acquaviva, *Member, IEEE*, and Enrico Macii, *Fellow, IEEE*

**Abstract**—This study presents a fully automated membrane segmentation technique for immunohistochemical tissue images with membrane staining, which is a critical task in computerized immunohistochemistry (IHC). Membrane segmentation is particularly tricky in immunohistochemical tissue images because the cellular membranes are visible only in the stained tracts of the cell, while the unstained tracts are not visible. Our automated method provides accurate segmentation of the cellular membranes in the stained tracts and reconstructs the approximate location of the unstained tracts using nuclear membranes as a spatial reference. Accurate cell-by-cell membrane segmentation allows per cell morphological analysis and quantification of the target membrane proteins that is fundamental in several medical applications such as cancer characterization and classification, personalized therapy design, and for any other applications requiring cell morphology characterization. Experimental results on real datasets from different anatomical locations demonstrate the wide applicability and high accuracy of our approach in the context of IHC analysis.

**Index Terms**—Cell segmentation, cellular membrane segmentation, image processing, immunohistochemistry (IHC), protein expression.

## I. INTRODUCTION

**D**IRECTLY monitoring the activity of proteins that are involved in the genesis and development of multifactorial genetic pathologies is a very useful diagnostic tool, which leads to the assessment of the characteristics of the pathology. For example, epidermal growth factor receptor (*EGFR*)/*erb-B* family of receptors plays an important role for a number of cancers, including lung, breast, colon, gastric cancer, etc.: quantifying and classifying the *EGFR* expression and activity with special regard to the assessment of the prevalence of *EGFR* mutations as well as to ligand–receptor interactions leads to new insights into the modulation of the receptor in individual carcinomas.

Moreover, the quantitative analysis of protein expression *in situ* in pathological tissues opens new opportunities for the design of novel targeted therapies through the definition of a group of potential candidates to protein family-inhibiting therapies.

Manuscript received August 2, 2010; revised November 7, 2010 and December 12, 2010; accepted December 12, 2010. Date of publication January 17, 2011; date of current version April 20, 2011. Asterisk indicates corresponding author.

E. Ficarra, A. Acquaviva, and E. Macii are with the Department of Control and Computer Engineering, Politecnico di Torino, Torino 10129, Italy (e-mail: elisa.ficarra@polito.it; andrea.acquaviva@polito.it; enrico.macii@polito.it).

\*S. Di Cataldo is with the Department of Control and Computer Engineering, Politecnico di Torino, Torino 10129, Italy (e-mail: santa.dicataldo@polito.it).

Color versions of one or more of the figures in this paper are available online at <http://ieeexplore.ieee.org>.

Digital Object Identifier 10.1109/TBME.2011.2106499

Thus, it is important to extract protein expression information by using methodologies that give quantifiable and standardized measurements [1].

One of the most prominent microscopy techniques in this field is immunohistochemistry (IHC) [2] that uses specific marked antibodies to stain proteins *in situ*. The analysis of stains' intensity and distribution at the specific location of interest targeted by the receptors (i.e., nuclei, cellular membranes, or cytoplasm of the cells, depending on the receptors) allows us to extract localized and highly specific protein expression information that is extremely useful for the assessment of the pathology [1].

In the last few years, IHC has acquired a central role in the field of pathology thanks to its several advantages over alternate bioimaging techniques, which include its wide availability, relatively low cost, and easy and long preservation of the stained slides [3]. With the goal of making pathologic examinations less subjective, the widespread use of IHC initially assisted pathologists only in making diagnoses, adding to or complementing morphological information with molecular information. More recently, it has been used to predict response to targeted therapy and to correlate protein and genetic expression data for improving therapies' accuracy [4] [see Fig. 1(a) for an example of the IHC tissue image].

This new role of IHC is placing new demands on the reproducibility, accuracy, and specificity of the extracted information [5]. In fact, IHC analysis has been traditionally performed by pathologists through direct visual inspection of micrographs of the specimens, which is extremely time-consuming, error-prone, and highly affected by inter- as well as by intraoperator variability [6], [7]; only recently the growing demand for automatization is being addressed by the main providers of systems for digital pathology, with dedicated software integrated to the IHC acquisition systems [3], [8], [9].

As recently acknowledged by modern pathology, for maximum relevance IHC should address per cell rather than per tissue analysis [10]: in fact, cells have been ultimately recognized as the fundamental units of behavior in multiple molecular pathways at the basis of pathology and cancer biology, so that the relevant metric in cancer development relies on their specific individual phenotypes [10]. This implies that the analytes are assessed in identifiable individual cells rather than on average in the whole tissue, which is not compatible with traditional visual evaluation. For this purpose, there is a growing demand for automated techniques able to identify cell by cell the specific location of interest of the studied receptors.

In this paper, we present an automated method for the cell-by-cell segmentation of cellular membranes in immunostained

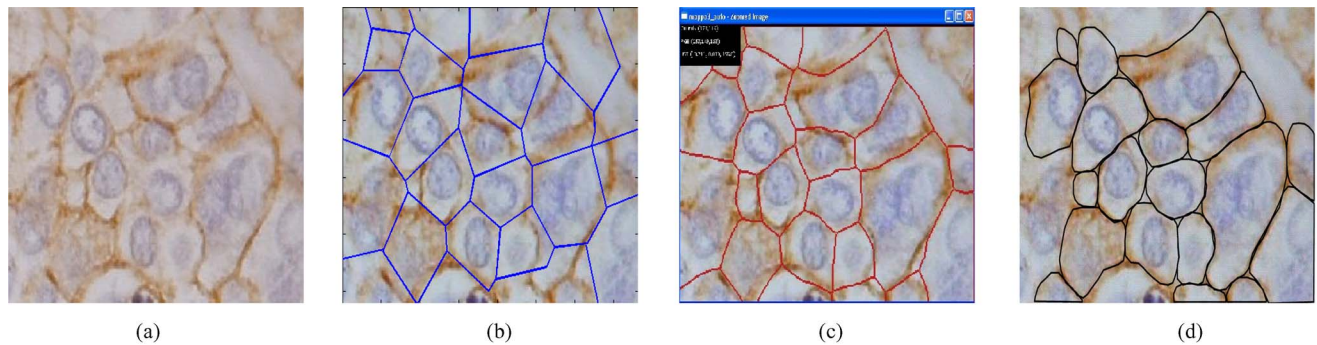


Fig. 1. Comparison between membrane approximation obtained through standard Voronoi tessellation and through our proposed labeling procedure (see Section II-A); cellular membranes manually traced by a pathologist are shown for reference. (a) IHC tissue image. (b) Standard Voronoi. (c) Labeling procedure. (d) Manual segmentation.

tissues, which is a highly critical task, especially in chromogenic IHC.

The most challenging issue is the reconstruction of the membranes in the portions that are negative to the target receptors (i.e., where protein activity is not present) that are not revealed by the stain and then not visible. The lack of intensity or gradient magnitude variations in the unstained parts of the membranes as well as the staining heterogeneity that is intrinsic of IHC imaging invalidate segmentation methods detecting intensity or gradient variations between the background and the pattern to be segmented [11]. Active contours approaches [12]–[14] overcome the problem of connecting broken contour lines by modeling the target pattern with a closed curve, but on the other hand they are extremely sensitive to initialization as well as to staining artifacts that may attract them far from the target membrane.

The largest amount of the literature in the field of cellular membrane segmentation addresses fluorescence or confocal microscopy images, where most of the challenges are related to the nonuniformity of the fluorescence signal, which may create variations and gaps in the membrane continuity. Interesting approaches have been proposed in this field: [15] presented a method based on Voronoi regions with a metric controlled by local image properties; [16] recently presented a generalized version of the subjective surfaces technique, while [17] used iterative tangential voting to enhance the protein bound signal followed by evolving fronts.

Very fewer techniques deal with automated membrane segmentation in chromogenic IHC, where different challenges arise due to the presence of unstained portions of the tissues (i.e., where the cells are negative to the target receptor and the membranes are not visible at all) and to the noise generated by the superposition and diffusion of different stains over the sample. Most of the recent works have been proved to be effective with nuclear segmentation but do not address cellular membranes' segmentation [18]–[20] or are semiautomated in that they need a certain amount of user intervention to add control points close to the target membrane boundary [21], [22]. Other recent works rely on elliptic approximation of the target membranes [23], [24], which does not reflect much the real morphology of several pathological tissues (see Fig. 1 for examples).

In this study, we present a method that provides fully automated segmentation of the cellular membranes in chromogenic IHC images, based on accurate detection of the stained tracts of the membranes and biologically realistic reconstruction of the unstained tracts using nuclear membranes as a spatial reference.

This paper is organized as follows. In Section II, we describe our fully automated procedure for cellular membrane segmentation. Section III reports the implementation details. In Section IV, we show experimental results that demonstrate the accuracy of our technique on real IHC images. Section V concludes this paper.

## II. MATERIALS AND METHODS

We analyzed histopathology images characterized by a blue stain (Hematoxylin, H) as background color and a brown stain (Diaminobenzidine, DAB) revealing the areas of the tissue where the target receptor as well as ligand of the target receptor family is detected; nevertheless, as explained later in Section II-B, our technique can be easily applied to IHC images with different histological stains. The images were acquired from different anatomical locations (i.e., lung, liver, and prostate cancer tissue). In particular, our experimental dataset included eight specimens acquired by different patients with resolutions spanning from 0.15 to 0.6  $\mu\text{m}/\text{pixel}$  and with membrane protein activation spanning from weak to very strong (see Section IV and Table II for a complete characterization). All the images were analyzed by a pathologist that provided manually segmented cellular membranes as ground truth to validate our procedure.

As outlined in Section I, computer-aided immunohistochemical analysis ideally requires to identify cell by cell the regions of the tissue that are targeted by the analyte (e.g., nuclei, cytoplasm, or cellular membranes); subsequently, it is possible to quantify the brown-colored areas at the identified location of interest.

In the case of images with membrane staining, this implies the accurate cell-by-cell segmentation of the cellular membranes in the tissue, which is the task addressed by our technique.

The brown stain reveals only the parts of the membranes that are positive to the target receptors; therefore, some cellular

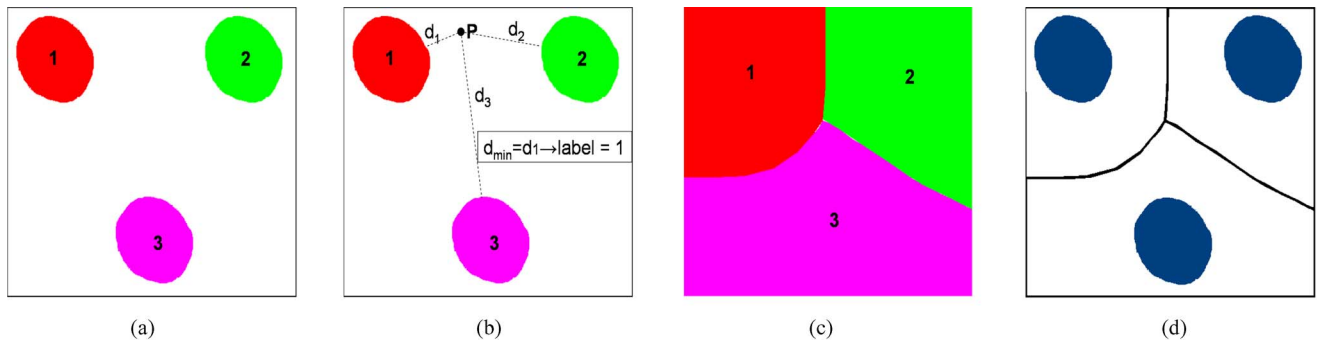


Fig. 2. Scheme of labeling procedure for the computation of approximate cell membranes: (a) regions are initialized with the points enclosed by the nuclear membranes; each region is characterized by a region label (1, 2, and 3 in this case) and represented by a different color; (b) each point  $P$  in the image is given the label of the closest nuclear membrane (in this case, label = 1); (c) final labeled regions; (d) approximate cell membranes obtained by outlining the labeled regions.

membranes may be totally unstained or either stained only in some tracts; only the stained tracts are visible and distinguishable from the background [see Fig. 1(a) for an example]. The amount of stained membranes as well as the continuity of the staining over the membranes is related to the characteristics and to the status of the pathology [25] and is not predictable *a priori*; in particular, in order to be able to quantify the continuity if the staining in terms of amount of stained membrane, the cellular membranes have to be reconstructed in both the stained (brown colored) and the unstained tracts.

This calls for nonstandard segmentation techniques working in the absence of intensity information coming from the unstained membranes' tracts (either absolute or in terms of gradient variation) and able to address staining inhomogeneity as well as nonpredictable shape variations of the cells; these variations may be induced by the pathology or by the mechanical and thermal stresses of the sample preparation [10]. These critical conditions invalidate the efficiency of popular segmentation methods in computer vision such as watersheds [26] and active contours [27], as well as any other method based either on intensity variations or fixed geometrical models of the patterns.

In our technique, we exploit the *detection of cellular membranes* by first reconstructing their approximate locations starting from nuclear membranes' profiles. This procedure, namely *computation of approximate cell membrane*, allows us to locate the most likely profiles of the cellular membranes in the tissue. Then we detect the brown parts of the membranes through color filtering and we connect them to the approximate cellular membranes in those regions of the cell that are negative to receptor reaction and then not visible. This procedure, namely *detection of final cellular membranes*, reconstructs cellular membranes even in the absence of intensity information, i.e., when membranes are partially or completely not visible in the image.

In the following sections, we provide a detailed description of our automated technique for membrane segmentation.

#### A. Computation of Approximate Cell Membranes

Approximate cell membranes are closed curves that resemble the locations of cellular membranes in the tissue; they are computed following a *minimum distance* criterion from nuclear membranes' profiles. This assumption is the most realistic from

a biological point of view since nuclei are generally located in the middle of the cell. On top of that, when the membrane is unstained, the location of the membrane can only be inferred from the position of the nuclei of the cells; therefore, the *minimum distance* criterion appears to be the most reasonable solution.

As shown in Fig. 1(a), unlike cellular membranes, the profile of nuclei is completely visible and delineated, so it can be used as a reliable spatial reference for cellular membranes detection. In our previous works addressing the problem of nuclear segmentation, we described and validated a fully automated morphology-based method that provides nuclear profiles in IHC tissue images; in this study, we used the nuclear profiles as a starting point for cellular membrane segmentation (see [28] and [29] for more details).

The literature reports several well-known tessellation approaches, which partition a given image into regions including points that are closer to a specific object, for example Voronoi diagrams [30] and Delaunay triangulation [31]; these approaches have been used in many different biological fields including models of cell growth as well as protein molecule volume analysis [32]. Standard Voronoi methods fix a discrete sets of points (e.g., the nuclei's barycenter) as the centers of tessellation, returning polygonal regions delimited by a number of edges dependent on the number and distribution of the nearest centers; in case the centers are few and regularly distributed, the polygonal regions are simple and delimited by few straight edges, as in the example of Fig. 1(b). Although the reference nuclei are the same as for standard Voronoi, the tessellation method used in our technique calculates distances from a set of smoothed curves rather than from individual centers, thus returning complex-shaped profiles that are a more realistic approximation of the cellular membranes [see Fig. 1(c) for examples].

In our tessellation approach, the *minimum distance* criterion from nuclear boundaries is exploited as follows (see Fig. 2): the image is partitioned in as many regions as the number of nuclei in the tissue. These regions are initialized by the set of pixels bounded by the nuclear membranes and are univocally identified by a region label [see Fig. 2(a)]. Then, a *labeling procedure* assigns each pixel in the image to one of the regions; in particular, each pixel is given a region label depending on the minimum distance between that pixel and the membranes of the surrounding nuclei, so that the pixel is finally assigned



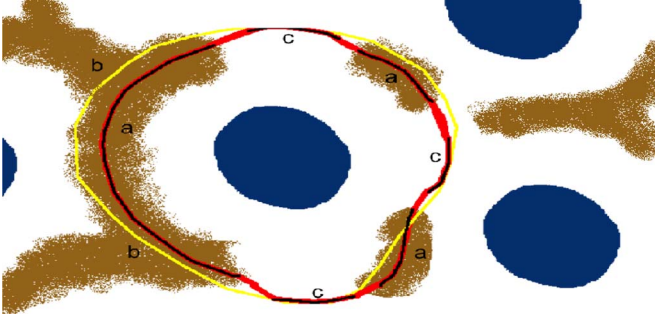


Fig. 3. Scheme of detection of final cellular membranes (please refer to the online version of the paper at <http://ieeexplore.ieee.org> for color coding). (a) Final membrane is computed as the barycenter curve of the brown-colored area and (b) forced to lie on the path that is closer to the nucleus to handle forks. (c) In the unstained tracts, the final membrane is forced to coincide with the approximate cell membrane, in yellow. Stained and unstained tracts of the final membrane are connected by a best fitting curve, in red.

to the region having the closest nucleus in it [see Fig. 2(b)]. Approximate cellular membranes are then obtained by outlining the boundaries of the final regions [see Fig. 2(c) and (d)].

The labeling process is based on detecting for each pixel in the image the closest nucleus, which requires to compute distances between points and nuclear membranes' profiles. Since a typical cancer tissue image may contain several hundreds of nuclear membranes with highly irregular profiles, this task may be computationally very intensive. In order to speed up this process, we implemented an optimized procedure that detects the closest nucleus to a given input point in the image in two sequential steps. In the first step, we perform a nearest-neighbor search to find the set of  $n$  nuclei closest to the input point. In particular, we approximate the nuclear membranes with their minimum bounding rectangles and we select the closest  $n$  nuclei based on the Euclidean distance between the input point and the vertices of the rectangles. See Section III for details about parameter  $n$ . In the second step, we select the closest nucleus among the previous  $n$ , this time based on the Euclidean distances calculated between the input point and *all* the points of nuclear membrane's profile. Therefore, the computation of the Euclidean distance between points and curves is limited to a small number of nuclei in the image, thus decreasing significantly the computational complexity of the labeling process.

### B. Detection of Final Cellular Membranes

The main steps of the final cellular membranes' detection are summarized in Fig. 3, where the approximate cell membrane and the final cellular membrane are represented in yellow and in red, respectively: 1) in the stained portions (labeled by *a*), we compute the red membrane as the barycenter curve of the brown-colored area; 2) at fork regions of the brown membrane (labeled by *b*), we force the red membrane to lie on the path that is closer to the nucleus of the cell through specific weighting coefficients in the barycenter's equation; 3) in the unstained portions of the membrane (labeled by *c*), we force the red membrane to coincide with the approximate cell membrane; 4) we refine the connection of the stained and the unstained portions by calculating a best fitting curve and removing outliers.

A detailed description of the procedure is provided as follows.

First of all, reactive membranes are detected through color filtering, highlighting the only brown-colored areas in the image. For this purpose, we used a specific color deconvolution algorithm [33] that was shown to achieve better results than other color segmentation methods, especially in IHC applications [34]. This method allows the separation not only of H and DAB (as in the case presented in this paper) but of all the standard histological stains [e.g., H-E, H, 3-amino-9-ethylcarbazole (AEC), etc.] as well as of any other stains, provided that their RGB vectors are experimentally determined and given as an input to the method (see [33] and [34] for details).

Then brown-colored membranes are connected to the approximate cell membranes in the nonreactive regions. For this purpose, the area across the approximate membrane, whose width  $w$  in pixels depends on image resolution (see Section III for details), is scanned by a scan line having one end on the pixel at the center of the nucleus and the other one on the pixel at the external border of the scanned area. (see Fig. 4); the cellular membrane is then reconstructed one pixel at a time as the weighted barycenter  $B$  of the brown pixels among the scan line, as in the following equation:

$$B = \frac{\sum_j c_j I_j j}{\sum_j c_j I_j} \quad (1)$$

where  $j$  is the pixel's coordinate along the scan line. This coordinate is 0 on the approximate membrane, negative in the inner part of the scanned area and positive in the outer part.  $I_j$  is the intensity value of pixel  $j$ , calculated as the complementary of the average RGB values and  $c_j$  is a coefficient for barycenter computation, calculated as follows:

$$c_j = \begin{cases} 1, & \text{if } j \leq 0 \\ 1 - kj, & \text{if } j > 0 \end{cases} \quad (2)$$

where  $k$  is a coefficient experimentally tuned (see Section III for details).

As shown in (2),  $c_j$  is equal to 1 for pixels with negative coordinate (i.e., closer to nucleus with respect to the approximate membrane); on the contrary, for pixels with positive coordinate  $c_j$  decreases linearly as the coordinate (i.e., the distance from the nucleus of the cell) increases. In this way, when the brown stain forks the membrane contour is forced to follow the path closest to the nucleus.

The intensity values of the background pixels are set to 0, whereas the intensity values of the scan-line's pixels that belong to or touch the approximate membrane are set to 1. In this way, in absence of brown pixels along the scan line, the barycenter  $B$  is forced to lie on the approximate membrane. As a consequence, the final cellular membrane coincides with the approximate membrane in the nonreactive (unstained) regions of the tissue. On the contrary, in the reactive regions of the tissue, brown pixels have intensity values much higher than 1 (ranging from 70 to 255), which always prevails in the computation of the barycenter. Therefore, the final cellular membrane is forced to lie on the pixels where the brown stain is more intense. Fig. 4 shows a picture of the *scanning procedure*.

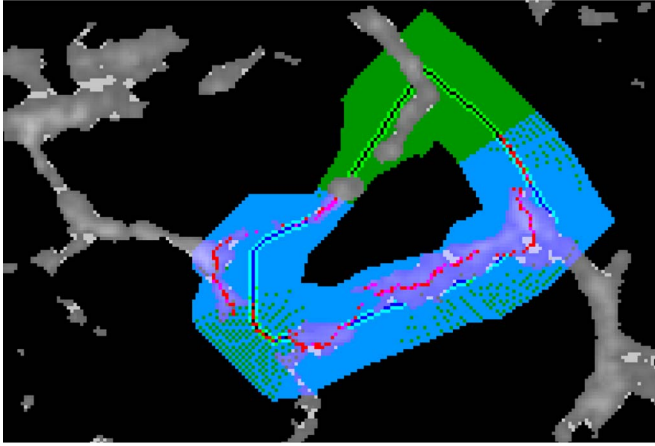


Fig. 4. Trace of scanning procedure (please refer to the online version of the paper at <http://ieeexplore.ieee.org> for color coding). Non reactive regions are in black, reactive membranes in gray; the area scanned by the scan line is shown in blue and green (blue if already scanned, green if yet to be scanned). In the middle of this area there is the approximate cellular membrane. At each step the barycenter of the brown pixels along the scan line is computed, obtaining the final cellular membrane (in red). In the nonreactive regions the final cellular membrane is forced to coincide with the approximate membrane.

TABLE I  
PARAMETERS' AND COEFFICIENTS' VALUES

Parameter	value
number of nuclei in nearest neighbour search ( $n$ )	4
width of the scanned area ( $w$ )	5.5 $\mu\text{m}$
coefficient of equation (2) ( $k$ )	0.0018

The second step of final cellular membranes' segmentation after the *scanning procedure* consists of an *iterative fitting procedure*, which refines the connection between stained and unstained tracts of the cellular membrane and iteratively deletes *outlier* pixels in the curve, which may be present due to local inhomogeneities of the brown stain. Outliers are pixels whose distance from the best fitting curve is more than three times the standard deviation, as in the traditional definition in statistics [35]. After removing the outliers, third-degree polynomial fitting is applied. Examples of final cell membrane detection are shown in Fig. 5.

### III. IMPLEMENTATION

The algorithm has been implemented in C++ inheriting the whole class hierarchy of the open-source *Cimg* public library [36]. The main parameters' values are reported in Table I. The width  $w$  of the area of the *scanning procedure* (see Section II-B) is related to the thickness of membrane staining in chromogenic IHC images; its value has been derived from the pathologists' observations and it is provided in  $\mu\text{m}$  in order to be resolution independent. The number of nuclei  $n$  in the nearest-neighbors search for the calculation of the distances between points and nuclear membranes' profiles (see the *labeling procedure* in Section II-A) was tuned in order to speed up the procedure for approximate cell membranes' computation without compromising the accuracy of membranes' approximation. Finally, the coefficient  $k$  of (2) (see *scanning procedure* for the detection of final cellular membranes in Section II-B) was empirically

TABLE II  
CHARACTERIZATION OF THE VALIDATION DATASETS

dataset	tissue	IHCscore	resolution	size	cells
1	lung	2+	0.6 $\mu\text{m}/\text{px}$	541x210	116
2	lung	2+	0.3 $\mu\text{m}/\text{px}$	279x237	38
3	lung	1+	0.3 $\mu\text{m}/\text{px}$	202x293	50
4	lung	1+	0.15 $\mu\text{m}/\text{px}$	345x236	27
5	lung	3+	0.3 $\mu\text{m}/\text{px}$	249x274	31
6	lung	1+	0.15 $\mu\text{m}/\text{px}$	507x609	46
7	liver	3+	0.4 $\mu\text{m}/\text{px}$	259x277	63
8	prostate	3+	0.15 $\mu\text{m}/\text{px}$	566x306	25

tuned in order to handle forks of the cellular membrane's profile and does not have to be adjusted by the user. All the values of the parameters reported in Table I are independent from image resolution as well as from image content.

### IV. EXPERIMENTAL RESULTS AND DISCUSSION

We tested our membrane segmentation technique for computer-aided protein activity quantification on eight datasets of real IHC images showing membrane stained cancer tissues from different anatomical locations, including lung nonsmall cell lung carcinoma (NSCLC), prostate and liver tissue. The eight datasets showed tissue specimens extracted from different patients and stained by H-DAB (see Fig. 8 for examples), including almost 400 cells. The images were acquired through brightfield digital microscopy at different enlargements; a complete characterization of the datasets, including the IHC score as provided by a pathologist according to the standard guidelines reported in [25], is provided in Table II.

We had all the cellular membranes in our datasets manually traced by a pathologist and we used manual segmentations as the ground truth to validate our segmentation method. We performed both a *direct validation* based on a pixel-wise distance metric between the automated and manual membranes, and an *indirect validation* based on the concordance between protein expression measures obtained from automated and manual membranes.

The *direct validation* is based on the computation of the *Hausdorff distance* [37], a well-known distance metric that measures the proximity between two sets of points by calculating the maximum distance between the first set and the nearest point of the second set: it is a severe metric that takes into account the maximum span between the two trajectories, instead of the average distance; moreover, it has been already used to validate membrane segmentation accuracy [16]. In our experiments, we calculated the *Hausdorff distance* between each automated membrane and the corresponding manual membrane, as follows:

$$d_H(A, M) = \max(\sup_{a \in A} \inf_{m \in M} d(a, m), \sup_{m \in M} \inf_{a \in A} d(a, m)) \quad (3)$$

where  $a$  and  $m$  are, respectively, the pixels belonging to the automated membrane  $A$  and the manual membrane  $M$  and  $d(a, m)$  is the Euclidean distance between  $a$  and  $m$ .

The results obtained in each validation dataset are reported in the boxplots of Fig. 6. It is a widely used representation technique in descriptive statistics where the boxes have horizontal lines at the three data distributions quartiles (the median value is

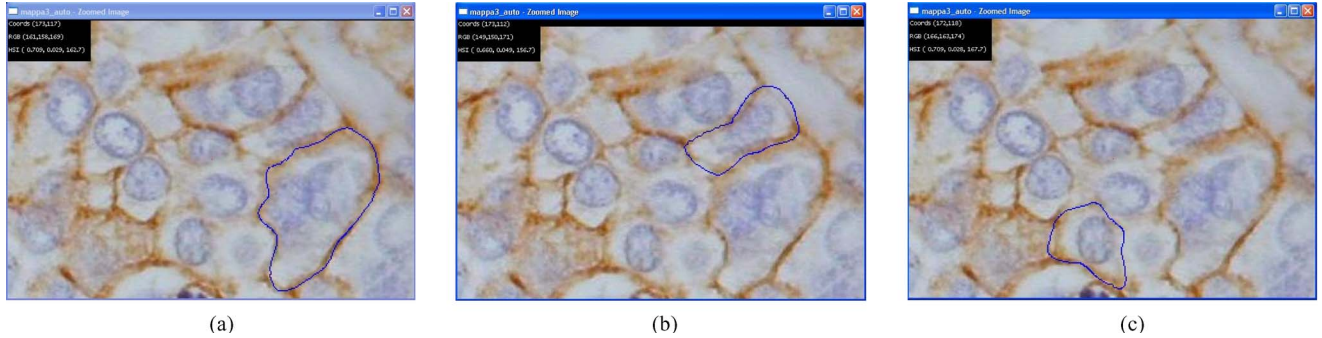


Fig. 5. Examples of membranes detection on *non-small cell lung carcinoma* (NSCLC) tissue immunohistochemical image. The final cellular membranes provided by our automated technique are highlighted in blue.

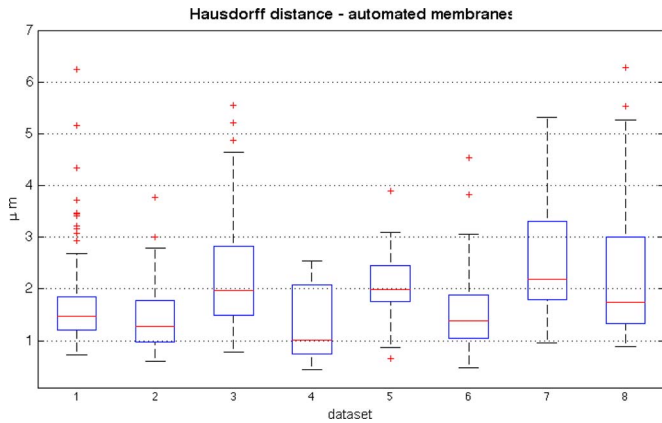


Fig. 6. Boxplot of Hausdorff distances between automated and manual membranes.

highlighted in red) and the vertical dotted lines show the extent of the data distribution.

We obtained distances between automated and manual membranes with a median value spanning between 1 and 2.2  $\mu\text{m}$ , and with a mean standard deviation of 0.95  $\mu\text{m}$ .

For a correct interpretation of the results, the intrinsic variability of the ground truth should be taken into account. In fact, the Hausdorff distance is extremely influenced by localized variations of the curve, which makes it a good metric of segmentation accuracy, provided that the reference curve is reliable enough. Therefore, it works well for applications where the manual operator is able to identify and trace the trajectory of cellular membranes with a high precision, as in [16]. In the specific application of chromogenic IHC, on the contrary, the Hausdorff distance may be strongly biased by the subjectivity and variability of the manual tracement. The reason of this variability is twofold: 1) in the stained portions of the tissue, the brown stain can be diffused over a large area over the cellular membrane, about 1–1.5  $\mu\text{m}$  thick (see Fig. 7, cell 1, as an example); 2) in the unstained portions of the tissue, the membranes are not visible; as a consequence, the manual tracement, besides being a realistic approximation derived from the experience of the pathologist, may be even more variable (see Fig. 7, cell 2).

In order to evaluate the variability of manual segmentations and its influence on the Hausdorff measure, we asked several operators (fifteen) to manually trace the cellular membranes of

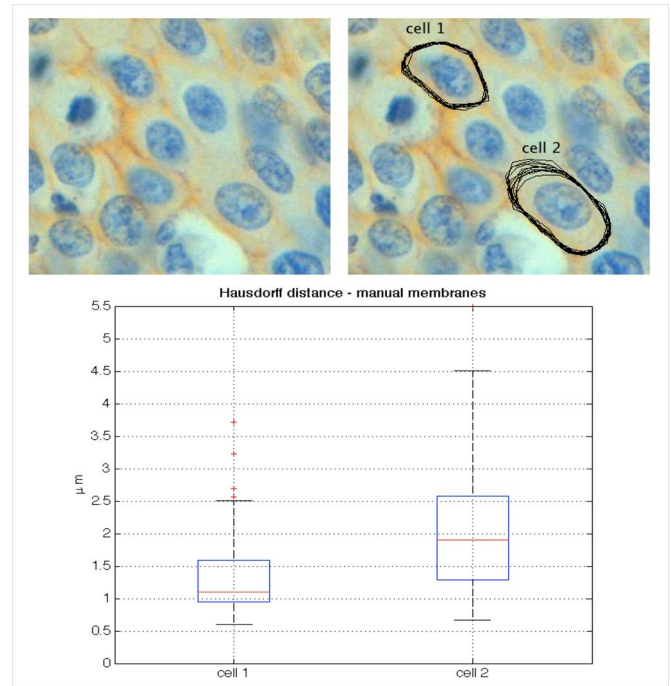


Fig. 7. Variability of manual-trace membranes in a cell with diffused brown staining (cell 1) and with unstained membrane (cell 2). The manual tracements provided by 15 operators are shown in black superimposed on the original image; the Hausdorff distances between each couple of manual-trace curve are reported in the boxplots below the images.

two sample cells, the former one with a well-delineated cellular membrane and the latter with a mostly unstained cellular membrane (shown in Fig. 7). Then, we calculated the Hausdorff distance between each couple of manually traced membranes, and reported the results in the boxplots of Fig. 7.

We obtained that manual measurements had a median Hausdorff distance of 1 and 1.9  $\mu\text{m}$ , respectively, in the stained and unstained cell, with standard deviations of 0.57 and 0.97  $\mu\text{m}$ , which show that the intrinsic variability of manual segmentations is comparable with the variability of the segmentations provided by our proposed automated approach. Since we verified that the pixel-wise evaluation is extremely biased by the variability of the manual tracement, especially in the unstained tracts; in our experiments, we also exploited an *indirect validation* that relies on the concordance between the protein expression



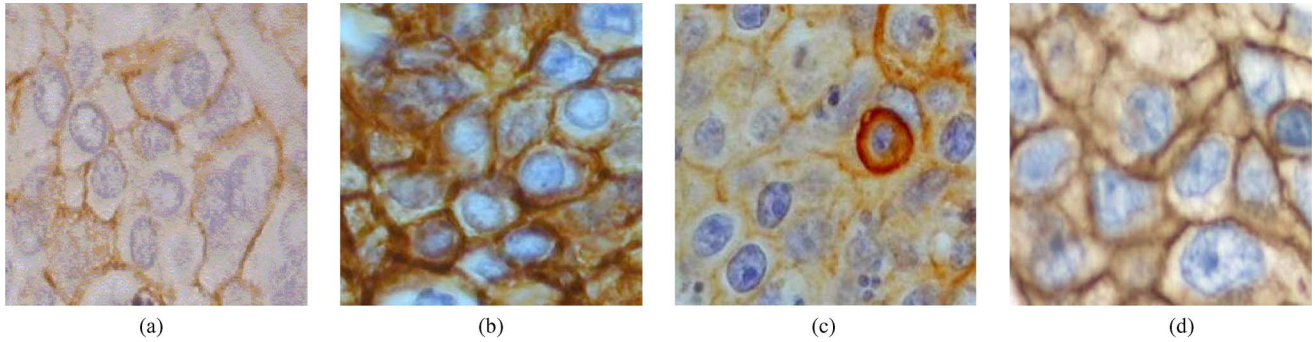


Fig. 8. Examples of immunohistochemical images used to validate our method (details).

evaluated along automated- and manually traced membranes, respectively. This metric does not rely on a pixel-by-pixel coincidence of the two trajectories and, therefore, it is less influenced by the intrinsic variability of the manual membrane; nevertheless, it is the best indicator of the similarity of the automated and manual membrane in the context of immunohistochemical analysis, which is the main target of membrane segmentation.

According to the recent guidelines by [25], membrane stained tissues are assigned a IHC score (from 0 negative to 3+ positive) depending on the overall intensity of the stain and on the *staining continuity* along the membrane. The latter feature, which is computed as the percentage of stained pixels along the cellular membrane (i.e., number of stained pixels divided by total number of pixels), is highly dependent on membrane segmentation: thus, in our study, we used staining continuity as an indirect indicator of membrane segmentation accuracy.

More specifically, for each dataset we performed a linear regression between measurements of *staining continuity* computed, respectively, along automated and manually traced membranes (taken as a reference) and we evaluated the statistical significance of the regression coefficient through *Student's t-test* [38].

Then, we computed the average error  $E_{AVG}$  and the rms error  $E_{RMSE}$  incurred by our automated approach with respect to ground truth consisting on the same measurements of staining continuity along manual-trace membranes, as follows:

$$E_{AVG} = \frac{1}{N} \sum |c_{auto} - c_{manual}| \quad (4)$$

$$E_{RMSE} = \sqrt{\frac{1}{N} \sum (c_{auto} - c_{manual})^2} \quad (5)$$

where  $c_{auto}$  and  $c_{manual}$  are the staining continuity calculated along automated and manual membranes, respectively, and  $N$  is the number of cellular membranes of the dataset.

Moreover, we computed the coefficient of correlation between the two sets of measurements by dividing the covariance of the two variables  $c_{auto}$  and  $c_{manual}$  by the product of their standard deviations, as reported in the following equation:

$$\rho_{auto,manual} = \frac{\text{Cov}(auto,manual)}{\sigma_{auto} \cdot \sigma_{manual}}. \quad (6)$$

This validation procedure evaluates the statistical equivalence of the two variables  $c_{auto}$  and  $c_{manual}$  and quantifies the statistical

TABLE III  
EXPERIMENTAL RESULTS ON COMPUTATION OF STAINING CONTINUITY ALONG CELLULAR MEMBRANES

dataset	Corr Coeff	Regr Coeff	Accept Reg	Av Err	RMSE
1	0.99	0.97	$\pm 0.34$	0.38	3.29
2	0.98	0.96	$\pm 0.096$	0.14	2.68
3	0.88	0.94	$\pm 0.20$	2.57	5.64
4	0.98	0.96	$\pm 0.108$	0.77	3.3
5	0.97	0.85	$\pm 0.11$	0.25	1.58
6	0.98	0.96	$\pm 0.09$	0.04	4.00
7	0.94	0.88	$\pm 0.12$	3.82	5.80
8	0.90	1.02	$\pm 0.36$	0.09	5.35

significance of this equivalence; the statistical equivalence of the two variables is an indirect indicator of the accuracy of membrane segmentation.

The results obtained in each validation dataset are reported in Table III; in particular, the second column reports the coefficient of correlation between automated and manual-trace measurements as in (6); third and fourth columns report the coefficient of the linear regression line and its region of statistical deviation with a 99% confidence level, respectively. The last two columns report the average of differences between automated- and manual-traced measurements (namely, average error) and the rms error (RMSE), respectively, calculated as in (4) and (5).

As shown in Table III, we obtained similar results in all the tested datasets. In particular, we found that our automated measurements were highly correlated with manual-traced measurements, with average coefficient of correlation 0.95. Moreover, we proved that automated and manual measurements were linearly correlated, with a regression coefficient close to one in six datasets out of eight and close to 0.9 in the remaining two datasets, and a narrow range of deviation. Average and rms errors with respect to manual measurement of staining continuity were below 3.82 and 5.80%, respectively, which is much below the resolution achievable by visual evaluation.

At last, we obtained that automated and manual-traced measurements were statistically equivalent in each of the validation datasets. This was proved by performing *Student's t-tests* on the difference between the two samples with a 99% confidence level.

As is shown by the examples reported in Fig. 5, the segmentations provided by our automated technique are accurate. Minor deviations from the stained boundary may arise due to local superposition of the reference nuclei with the target

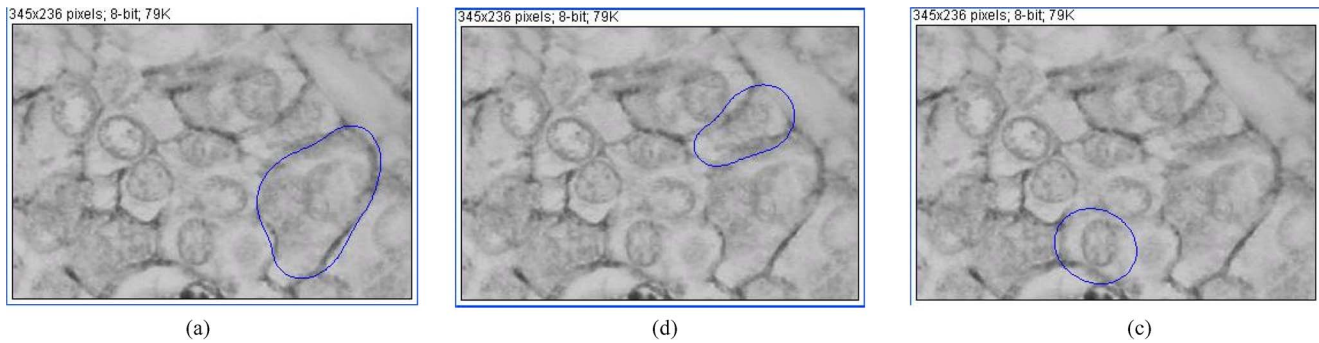


Fig. 9. Examples of membranes detection using active contours approach.

membrane or due to missing reference nuclei [e.g., left tract of cell in Fig. 5(c)]; these artifacts may be generated by the superposition of different tissue layers, diffusion of the dye partially or completely hiding the nuclei and tissue deformations happening during the preparation of the sample. Nevertheless, our quantitative validation demonstrates that our technique copes well with all the issues of IHC segmentation and provides results that are statistically comparable with manual segmentations.

In order to compare the results obtained by our technique with other popular automated approaches, we made additional experiments with active contours, a well established segmentation method in computer vision as well as in medical imaging that addresses gradient as well as spatial intensity information [27]. Active contours have the inherent capability of modeling the target object through a closed curve: thus, they overcome the problem of connecting broken contour lines that is a major limitation in other widespread edge-based or region-based segmentation techniques. In fact, as anticipated in Section I several formulations of active contours have been applied to the task of cell segmentation. Nevertheless, active contours' performance is extremely affected by curve initialization, as well as by heterogeneous staining and presence of foreign particles in the tissue which may attract the curve far from the target membrane.

In this study, we implemented a semiautomated segmentation technique using the active contours presented by [39] that were initialized by an operator close to the targeted cellular membranes. Moreover, in order to decrease the influence of wrong curve attractors in the images, we preventively performed both noise- and color filtering. More details about the implementation of the active contours for IHC image segmentation are provided in our previous work [29]. We run experiments in a lung cancer tissue dataset, measuring the performance of the automated segmentation versus manual segmentation through the aforementioned indirect validation based on the staining continuity. The results obtained by active contours approach and the results obtained in the same dataset by our automated technique are reported in Table IV for comparison.

In Fig. 9, we show examples of cell membrane detection obtained by active contours approach. The segmentation provided by our proposed method on the same cellular membranes was already shown in Fig. 5. The superiority of our method over active contours approach is fairly evident from the quantitative results as well as from visual evaluation.

TABLE IV  
EXPERIMENTAL RESULTS ON COMPUTATION OF STAINING CONTINUITY ALONG CELLULAR MEMBRANES IN A LUNG CANCER TISSUE SAMPLE

	Corr Coeff	Av Err	RMSE
active contours	0.629	23.44	26.44
proposed	0.98	0.14	2.68

Results obtained by active contours and by our proposed technique are reported in the first and second row, respectively.

## V. CONCLUSION

We presented a fully automated membrane segmentation approach that allows the quantification of the expression of membrane receptors in cancer tissue images, which is usually performed by pathologists via visual inspection of the samples. Our technique streamlines this error-prone and time-consuming process, thereby facilitating analysis and diagnosis as well as the design of novel targeted therapies. The automated segmentation of cellular membranes as provided by our method leads to the analysis of membrane protein activity *in situ* on a cell-by-cell basis, which is critical for the accurate assessment of a number of important pathologies; moreover, it allows any other application that relies on accurate tissue and cell exploration in IHC tissue images. In particular, our technique overcomes the limitations of traditional segmentation techniques based on local or spatial intensity information as well as gradient magnitude variation. The effectiveness and robustness of the proposed method have been tested on real immunohistochemical images from several tissue locations, including lung, prostate, and liver tissue. Results of comparison with ground truth provided by pathologists on several real-life datasets demonstrate the high accuracy of our approach in the context of IHC analysis.

## ACKNOWLEDGMENT

The authors would like to thank Dr. M. Volante and his collaborators of Hospital S. Luigi of Orbassano, Torino, Italy, for providing the images and as well as for the helpful discussion.

## REFERENCES

- [1] T. K. Taneja and S. K. Sharma, "Markers of small cell lung cancer," *World J. Surg. Oncol.*, vol. 2, p. 10, 2004.
- [2] Z. Ahmed, N. S. Azad, Y. Bhurgari, R. Ahmed, N. Kayani, S. Pervez, and S. Hasan, "Significance of immunohistochemistry in accurate characterization of malignant tumors," *J. Ayub. Med. Coll. Abbottabad.*, vol. 18, pp. 38–43, 2006.



- [3] Z. Theodosiou, I. Kasampalidis, G. Livanos, M. Zervakis, I. Pitas, and K. Lyroudia, "Automated analysis of fish and immunohistochemistry images: A review," *Cytometry A*, vol. 71, pp. 459–450, 2007.
- [4] M. J. Borad, R. Penny, M. Bittner, J. Gardner, S. Shack, E. Campbell, D. Taverna, R. Love, J. Trent, and D. V. Hoff, "Molecular profiling using immunohistochemistry (IHC) and dna microarray (DMA) as a tool to determine potential therapeutic targets in patients who have progressed on multiple prior therapies," in *Proc. 1st Amer. Assoc. Cancer Res. (AACR) Int. Conf. Mol. Diagnost. Cancer Therapeutic Development*, Abstract B82, 2006.
- [5] M. Cregger, A. J. Berger, and D. Rimm, "Immunohistochemistry and quantitative analysis of protein expression," *Arch. Path. Lab. Med.*, vol. 130, pp. 1026–1030, 2006.
- [6] M. Lacroix-Triki, S. Mathoulin-Pelissier, J. Ghnassia, G. Macgrogan, A. Vincent-Salomon, V. Brouste, M. Mathieu, P. Roger, F. Bibeau, and J. Jacquemier, "High inter-observer agreement in immunohistochemical evaluation of her-2/neu expression in breast cancer: A multicentre gepcips study," *Eur. J. Cancer*, vol. 42, pp. 2946–2953, 2006.
- [7] J. P. Sloane, I. Amendoeira, N. Apostolikas, J. P. Bellocq, S. Bianchi, W. Boecker, G. Bussolati, D. Coleman, C. E. Connolly, P. Dervan, V. Eusebi, C. D. Miguel, M. Drijkoningen, C. Elston, D. Faverley, J. J. A. Gad, M. Lacerda, J. Martinez-Penuela, C. Munt, J. L. Peterse, F. Rank, M. Sylvan, V. Tsakraklides, and B. Zafrani, "Consistency achieved by 23 european pathologists in categorizing ductal carcinoma in situ of the breast using five classifications. european commission working group on breast screening pathology," *Hum. Pathol.*, vol. 29, pp. 1056–1062, 1998.
- [8] K. A. Divito and R. L. Camp, "Tissue microarrays—automated analysis and future directions," *Breast Cancer Online*, vol. 8, pp. 1–5, 2005.
- [9] M. G. Rojo, G. Bueno, and J. Slodkowska, "Review of imaging solutions for integrated quantitative immunohistochemistry in the pathology daily practice," *Folia Histochem. Cytobiol.*, vol. 47, pp. 349–354, 2009.
- [10] C. R. Taylor and R. M. Levenson, "Quantification of immunohistochemistry—Issues concerning methods, utility and semiquantitative assessment II," *Histopathology*, vol. 49, pp. 411–424, 2006.
- [11] N. Malpica, C. de Solrzano, I. J. Vaquero, A. Santos, I. Vallcorba, J. Garca-Sagredo, and F. del Pozo, "Applying watershed algorithms to the segmentation of clustered nuclei," *Cytometry*, vol. 28, pp. 289–297, 1997.
- [12] L. Yang, P. Meer, and D. J. Foran, "Unsupervised segmentation based on robust estimation and color active contour models," *IEEE Trans. Inf. Technol. Biomed.*, vol. 9, no. 3, pp. 475–486, Sep. 2005.
- [13] D. P. Mukherjee, N. Ray, and S. T. Acton, "Level set analysis for leukocyte detection and tracking," *IEEE Trans. Image Process.*, vol. 13, no. 4, pp. 562–572, Apr. 2004.
- [14] A. Elmoataz, S. Schupp, R. Clouard, P. Herlin, and D. Bloyet, "Using active contours and mathematical morphology tools for quantification of immunohistochemical images," *Signal Process.*, vol. 71, pp. 215–226, 1998.
- [15] T. R. Jones, A. Carpenter, and P. Golland, "Voronoi-based segmentation of cells on image manifolds," *Lect. Notes Comput. Sci. (LNCS)*, vol. 3765, pp. 535–543, 2005.
- [16] C. Zanella, M. Campana, B. Rizzi, C. Melani, G. Sanguinetti, P. Bourguine, K. Mikula, N. Peyrieras, and A. Sarti, "Cells segmentation from 3-d confocal images of early zebrafish embryogenesis," *IEEE Trans. Image Process.*, vol. 19, no. 3, pp. 770–781, Mar. 2010.
- [17] J. Han, H. Chang, K. Andarawewa, P. Yaswen, M. H. Barcellos-Hoff, and B. Parvin, "Multidimensional profiling of cell surface proteins and nuclear markers," *IEEE/ACM Trans. Comput. Biol. Bioinf.*, vol. 7, no. 1, pp. 80–90, Jan.–Mar. 2010.
- [18] T. Markiewicz, C. Jochymski, R. Koktycz, and W. Kozłowski, "Automatic cell recognition in immunohistochemical gastritis stains using sequential thresholding and SVM network," in *Proc. 5th IEEE Int. Symp. Biomed. Imag. (ISBI)*, 2008, pp. 971–974.
- [19] P. Phukpattaranont and P. Boonyaphiphat, "Computer-aided analysis of nuclear stained breast cancer cell images," in *Proc. 5th Int. Conf. Electr. Eng./Electron., Comput., Telecommun. Inf. Technol. (ECTI-CON)*, 2008, pp. 485–488.
- [20] C. Hang, R. A. DeFilippis, T. D. Tlsty, and B. Parvin, "Scoring histological sections through immunohistochemistry," in *Proc. 5th IEEE Int. Symp. Biomed. Imag. (ISBI)*, 2008, pp. 344–347.
- [21] C. Sun, P. Vallotton, D. Wang, J. Lopez, Y. Ng, and D. James, "Membrane boundary extraction using circular multiple paths," *Pattern Recog.*, vol. 42, pp. 523–530, 2009.
- [22] D. Baggett, M. A. Nakaya, M. McAuliffe, T. P. Yamaguchi, and S. Lockett, "Whole cell segmentation in solid tissue sections," *Cytometry A*, vol. 67, pp. 137–143, 2005.
- [23] M. A. Gavrielides, H. Masmoudi, N. Petrick, K. J. Myers, and S. M. Hewitt, "Automated evaluation of her-2/neu immunohistochemical expression in breast cancer using digital microscopy," in *Proc. 5th IEEE Int. Symp. Biomed. Imag. (ISBI)*, 2008, pp. 808–811.
- [24] H. Masmoudi, S. M. Hewitt, N. Petrick, K. J. Myers, and M. A. Gavrielides, "Automated quantitative assessment of her-2/neu immunohistochemical expression in breast cancer," *IEEE Trans. Med. Imag.*, vol. 28, no. 6, pp. 916–925, Jun. 2009.
- [25] A. C. Wolff, M. E. Hammond, J. N. Schwartz, K. L. Hagerty, D. C. Allred, R. J. Cote, M. Dowsett, P. L. Fitzgibbons, W. M. Hanna, A. Langer, L. M. McShane, S. Paik, M. D. Pegram, E. A. Perez, M. F. Press, A. Rhodes, C. Sturgeon, S. E. Taube, R. Tubbs, G. H. Vance, M. van de Vijver, T. M. Wheeler, and D. F. Hayes, "American society of clinical oncology/college of American pathologists guideline recommendations for human epidermal growth factor receptor 2 testing in breast cancer," *Arch. Pathol. Lab. Med.*, vol. 131, pp. 18–43, 2007.
- [26] J. B. T. M. Roerdink and A. Meijster, "The watershed transform: Definitions, algorithms and parallelization strategies," *Fund. Inf.*, vol. 41, pp. 187–228, 2001.
- [27] M. Kass, A. Witkin, and D. Terzopoulos, "Snakes: Active contours models," *Int. J. Comput. Vis.*, vol. 1, pp. 321–331, 1987.
- [28] S. D. Cataldo, E. Ficarra, and E. Macii, "Selection of tumor areas and segmentation of nuclear membranes in tissue confocal images: A fully-automated approach," in *Proc. IEEE Int. Conf. Bioinform. Biomed. (BIBM)*, 2007, pp. 390–398.
- [29] S. D. Cataldo, E. Ficarra, A. Acquaviva, and E. Macii, "Segmentation of nuclei in cancer tissue images: Contrasting active contours with morphology-based approach," in *Proc. IEEE 8th Symp. Bioinform. Bioeng. (BIBE)*, 2008, pp. 1–6.
- [30] F. Aurenhammer and R. Klein, "Voronoi diagrams," in *Handbook of Computational Geometry*, J. Sack and G. Urrutia, Eds. Amsterdam, The Netherlands: Elsevier, 2000, pp. 201–290.
- [31] K. Fukuda. (2004). Frequently asked questions in polyhedral computation [Online]. Available: <http://www.ifor.math.ethz.ch/~fukuda/polyfaq/polyfaq.html>.
- [32] A. R. Kansal and T. S. Deisboeck, "Simulated brain tumor growth dynamics using a three-dimensional cellular automaton," *J. Theor. Biol.*, vol. 203, pp. 367–382, 2000.
- [33] A. C. Ruifrok and D. A. Johnston, "Quantification of histochemical staining by color deconvolution," *Anal. Quant. Cytol. Histol.*, vol. 23, pp. 291–299, 2001.
- [34] A. Ruifrok, R. Katz, and D. Johnston, "Comparison of quantification of histochemical staining by hue-saturation-intensity (HSI) transformation and color deconvolution," *Appl. Immunohistochem. Mol. Morphol.*, vol. 11, pp. 85–91, 2004.
- [35] P. Sun and S. Chawla, "On local spatial outliers," in *Proc. IEEE Int. Conf. Data Mining (ICDM)*, 2004, pp. 209–216.
- [36] D. Tschumperl. The Cimg library. (2010). [Online]. Available: <http://cimg.sourceforge.net>
- [37] J. Munkres, *Topology*. Englewood Cliffs, NJ: Prentice-Hall, 1999.
- [38] J. H. Zar, *Biostatistical Analysis*. Englewood Cliffs, NJ: Prentice-Hall, 1999.
- [39] M. Jacob, T. Blu, and M. Unser, "Efficient energies and algorithms for parametric snakes," *IEEE Trans. Image Process.*, vol. 13, no. 9, pp. 1231–1244, Sep. 2004.

Author's photograph and biography are not available at the time of publication.